Radiative sky cooling of solar cells: fundamental modelling and cooling potential of single-junction devices

Jérémy Dumoulin, Emmanuel Drouard, Mohamed Amara

RADIATIVE SKY COOLING OF SOLAR CELLS: FUNDAMENTAL MODELLING AND COOLING POTENTIAL OF SINGLE-JUNCTION DEVICES

Jérémy Dumoulin
Institut des Nanotechnologies de Lyon, UMR5270, Univ. Lyon, INSA de Lyon, CNRS, F-69621 Villeurbanne, France

Emmanuel Drouard
Institut des Nanotechnologies de Lyon, UMR5270, Univ. Lyon, Ecole Centrale de Lyon, F-69130 Ecully, France

Mohamed Amara
Institut des Nanotechnologies de Lyon, UMR5270, Univ. Lyon, INSA de Lyon, CNRS, F-69621 Villeurbanne, France
mohamed.amara@insa-lyon.fr

ABSTRACT

Data mining is a good way to find the relationship between raw data and predict the target we want which is also widely used in different field nowadays. In this project, we implement a lots of technology and method in data mining to predict the sale of an item based on its previous sale. We create a strong model to predict the sales. After evaluating this model, we conclude that this model can be used in normal life for future sale's prediction. Radiative sky cooling is a promising method to passively cool photovoltaic cells under outdoor conditions, thus improving their power conversion efficiency along with their lifetime. Analyses for some devices have suggested temperature reductions of several degrees thanks to this method, but they remain insufficient to estimate the cooling potential for different technologies according to their basic electrical and thermal properties. Furthermore, the ideal thermal emissivity profile that permits the best cooling has never been studied in detail. This paper investigates the effect of radiative sky cooling on single-junction solar cells from a general perspective. A numerical model based on detailed-balance theory and heat balance allows us to estimate the temperature and the electrical power output for different cells. A focus is made on devices based on three representative solar absorber materials: silicon, gallium arsenide, and perovskite. We first demonstrate that a broadband emissivity profile (a blackbody-like emissivity) overcomes the performance of a selective emissivity profile (with a non-zero emissivity only in the 8 μm to 13 μm atmospheric window) in most scenarios. Secondly, we quantify the potential of this ideal emissivity profile in terms of temperature reduction and electrical power enhancement. We study the influence of both the thermal emission and sub-band gap parasitic solar absorption on thermal management. This allows us to predict the possible performance enhancement of a device according to its initial emissivity profile. Material specific effects such as band gap dependance with temperature and non-radiative recombination are also discussed. The sensitivity to heat exchange on the rear and sides of a device is quantified. This study provides a fundamental basis for radiative sky cooling of photovoltaic cells and a guideline for further simulation-based studies.

1 Introduction

The energy conversion efficiency of single-junction photovoltaic (PV) cells has increased considerably over the years, reaching 26.7% [1] for silicon (Si) solar cells under standard testing conditions (25 °C, 1000 W.m^{-2} with the reference AM 1.5 spectrum). However, their efficiency remains intrinsically limited to $\sim$33% by detailed-balance theory [2].

For silicon-based cells, the theoretical limit is even lower (29.4% [3]). While solar cells absorb most incident solar energy, this results in a significant heating of the cells and of the entire solar module. Under outdoor conditions, Si modules typically reach 50-60 °C [4]. These high temperatures cause efficiency and reliability issues, leading to a reduced energy output over the module's lifetime. For most technologies, the conversion efficiency is decreasing when the cell temperature rises. For example, the relative efficiency loss of crystalline silicon cells is about 0.45% for every 1 °C increase [5]. High temperatures also accelerate degradation: it was reported that the ageing rate doubles for each 10 °C increase [6]. Thus, there is considerable interest in developing cooling strategies for PV devices. Conventional PV cooling technologies include natural and forced ventilation, hydraulic cooling, heat pipe, phase-change materials and thermoelectric cooling [7, 8, 9, 10, 11]. However, most of them require extra energy input or significantly increase the system complexity.

In recent years, there has been growing interest in the radiative sky cooling (RSC) strategy. As PV systems have a large surface area oriented towards the sky, they are naturally good candidates for this technique, which uses the transparency of the earth's atmosphere in the 8-13 μm range in order to enhance radiative heat transfer [12, 13, 14]. In practice, improving RSC consists in tuning the optical absorption and thermal emission in the infrared range which makes it possible to also reduce the absorption of sub-band gap photons, referred hereafter as parasitic solar absorption. Such photons, which can be present up to $\sim$4 μm, cannot be converted into electricity and represent a parasitic heat source. Based solely on the optimisation of the optical properties, the RSC strategy thus allows to passively cool solar cells by controlling both radiative heat transfer with the sky and parasitic solar absorption. It is known to have an impressive cooling potential [14]: by suppressing non-radiative heat transfer and minimising solar radiation by using a sun shade, a multi-layer photonic structure has been cooled down to 42 °C below the ambient temperature [15]. However, as PV systems exhibit specific constraints, it is not yet clear what the cooling potential is and what are the pathways to fully exploit it.

Zhu et al [17] showed in 2014 that a 2D photonic crystal could lower the operating temperature of a doped crystalline silicon wafer by about 18 °C. Experimentally, a cooling of nearly 13 °C was achieved in 2015[18], and Long et al [19] also demonstrated a 2 °C temperature reduction under outdoor conditions. The aforementioned studies were conducted on silicon wafers, not on operational cells, but simulations from An et al [20] predict a 10 °C reduction also for thin silicon cells operating at maximum power point. Safi et al [21] suggest that cells made from materials with a higher band gap energy than silicon could operate even below ambient temperature through enhanced RSC. On the other hand, Gentle and Smith [22] noticed that the starting point for studies should be the solar module, not only the cell. Their simulations suggest that enhanced RSC of standard silicon modules could only provide less than 2 °C additional temperature reduction. Nonetheless, parasitic solar absorption were not taken into account in their approach. Simulations of silicon modules performed by Li et al [23] showed that a decrease of 9 °C is possible if parasitic solar absorption were entirely suppressed. Sun et al [24] have studied the influence of this effect on different solar module technologies. Their study confirms that, for Si-based device, a cooling of only 2 °C is possible if parasitic solar absorption remain unsuppressed. When suppressed, the cooling reaches 6 °C. The cooling potential is higher for the CdTe device considered in their study (10 °C), but lower for the GaAs module (2 °C).

This wide variability in the predicted cooling potential is related to several factors:

1. The considered solar technology and the modelling hypothesis. For instance, many studies do not take into account the coupling between electrical and thermal properties although the latter is intrinsically present in any solar cell. It must be considered to estimate the cell temperature at maximum power point, which can differ from the temperature in open-circuit by several degrees [25, 26].

2. The thermal emissivity profiles used as starting and ending points. In fact, the initial emissivity contributing to radiative cooling strongly depends upon technologies, and thus the potential predicted through further optimisation: measured absorption spectra on different solar absorber materials shows, for example, that parasitic absorption can be much higher for Si-based than for GaAs-based devices [24]. Moreover, the absorption/emission profile is affected by the encapsulation layers [23] or the cell's architecture [27, 28]. It is also not clear at this time which emissivity profile should be used to get the best out of radiative sky cooling. In fact, two profiles are generally presented in literature [29, 30, 31]: a broadband profile with unity thermal absorption/emission above $\sim$4 μm and zero below in order to suppress unwanted solar absorption, and a selective profile with a thermal absorption/emission restricted to the main atmospheric transparency window. The absorbed and the emitted radiation from a surface for both profiles is shown in figure 1. To the best of our knowledge, whether the one or the other is the ideal emissivity profile has never been studied in detail.

3. Environmental conditions used as inputs (solar irradiance, atmospheric irradiance, level of convection relative to wind speed, ambient temperature). For example, several studies use the AM1.5 standard spectrum with an atmospheric irradiance computed from the Gemini observatory data [32]. However, this combination is not

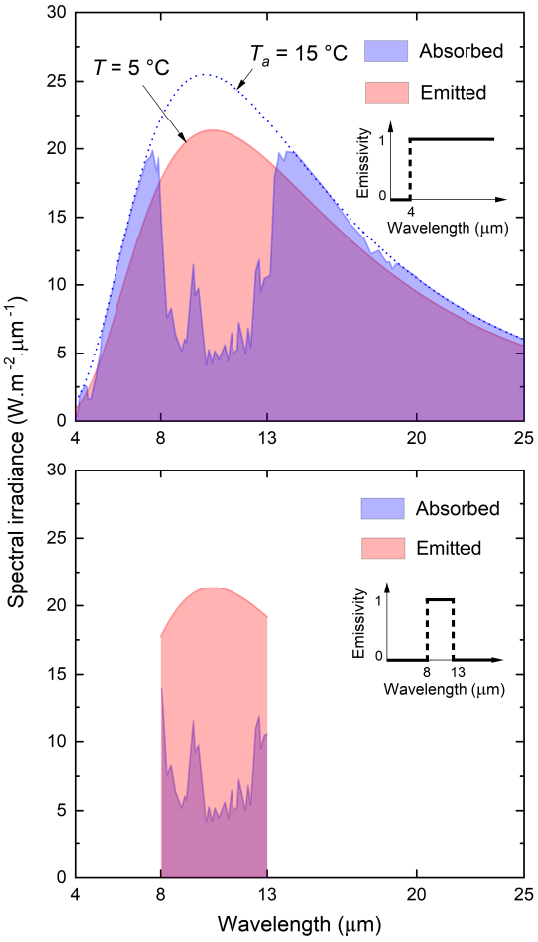

Figure 1: Absorbed and emitted atmospheric irradiance of a cell with a broadband (top) and a selective (bottom) thermal emissivity. For illustration purpose, we assume an ambient temperature T_a = 15 °C and a cell operating at T = 5 °C. The dotted line of the graph on the left shows the thermal emission of a black body at 15 °C. The absorbed irradiance (blue) corresponds to the US standard atmosphere [16].

close to realistic operating conditions since the standard solar spectrum is based on the US standard atmosphere [33].

In this paper, we propose a general framework to study RSC based on a fundamental thermoelectric model of single-junction solar systems. We also introduce reference climatic conditions to estimate the potential of RSC close to real operating conditions. Our approach aims to explain, describe, and predict the impact of RSC on the temperature and also on the electrical output for a wide variety of single-junction devices, by avoiding material and design peculiarities as a first step. Although based on basic assumptions, it includes the specificities of PV systems that must be taken into account to assess their thermoelectric behaviour. Indeed, PV systems are out-of-equilibrium systems where part of the absorbed solar energy is converted into work and where luminescent radiation is present. As mentioned above, the coupling between thermal and electrical properties must be considered to estimate the cell temperature. It is also important to take into account a possible change in the temperature coefficient, which may, for example, arise from a change in band-to-band absorption properties [34].

We first use our model to assess the ideal emissivity profile for single-junction PV devices. Then, we determine the potential benefit of the latter for solar cells with three different band gap energies, representative of relevant technologies: silicon (Si), gallium arsenide (GaAs), and methylammonium lead iodide perovskite ($CH_3NH_3PbI_3$), referred hereafter as perovskite. The benefit, expressed in terms of temperature decrease and electrical power enhancement, is computed as a function of the initial emissivity profile of the device in order to estimate the potential for a wide range of solar

cells/modules. The influence on this potential of band gap change with temperature, non-radiative recombination, and imperfect band-to-band absorption is studied. Finally, the effect of heat transfer that occur at the rear and sides of the PV device is also quantified.

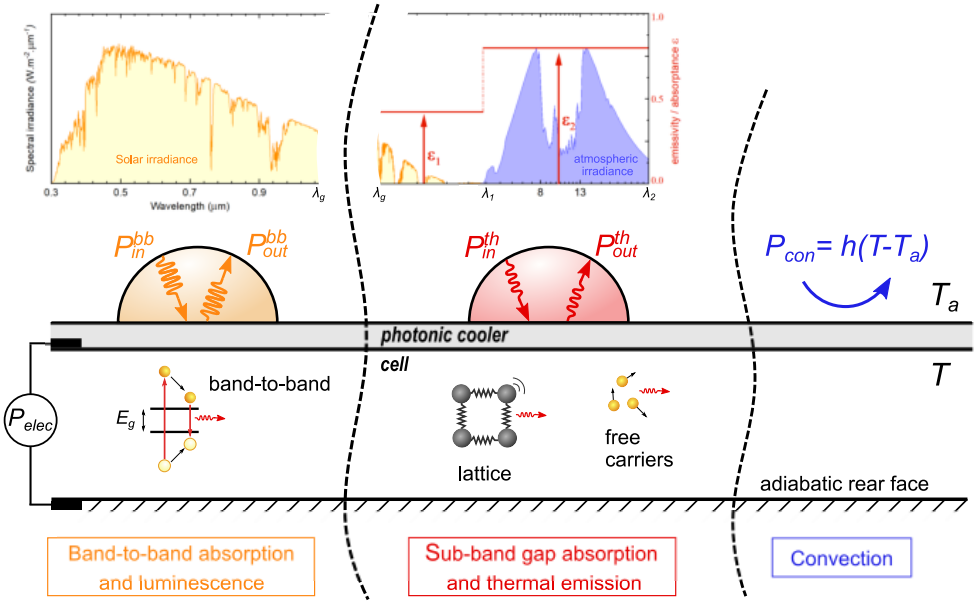

Figure 2: Problem schematic description with the parameters of the model.

2 Methods

In this section, we: 1) formulate the thermoelectric model used to compute the temperature and the electrical output of the solar cell from environmental conditions; 2) introduce a "step-model" for the emissivity profile that allows us to decouple the contribution of parasitic solar absorption and radiative exchange with the atmosphere; 3) describe and justify the reference conditions chosen in this work in order to estimate the potential benefit of enhanced RSC, i.e. its ability to lower the device temperature and increase its electrical power output.

The presented model describes the thermoelectric behaviour of single-junction cells with ideal electrical and optical properties. An extended model is presented in the appendix to study the influence of other major effects present in real solar cells in a second stage, such as band gap change with temperature, non-radiative recombination, imperfect band-to-band absorption, and heat transfer on the rear side.

2.1 Thermoelectric modelling

The electrical output power is calculated using a detailed-balance approach, in combination with a heat balance model to obtain the operating temperature. Steady state conditions and perfect impedance matching are assumed, so that the solar cell is operating at maximum power point (MPP). To assess the latter we first calculate the current-voltage characteristic while finding the equilibrium temperature for each voltage. Then, the MPP is extracted.

Solar cell models derived from the principle of detailed-balance are powerful to gain insights on many phenomenon, by describing a near-ideal solar cells with a restricted set of parameters. In the classical Shockley-Queisser approach, the band gap energy E_g is the only parameter [2]. Assuming purely radiative band-to-band recombination, perfect absorption of photons with energies above the band gap, one electron-hole pair per absorbed photon, ideal selective contacts and no resistive losses, the produced surface power density P_{elec}, is expressed via

$$P_{elec} = qV \int_{E_g}^{\infty} (\phi_{in}(E) - \phi_{em}(E,T,V)) \frac{dE}{E} \tag{1}$$

with V being the internal voltage, q the elementary charge, E_g the band gap energy, T the cell temperature, E the photon energy. As there is no fundamental dependency between the band gap energy and the temperature, a constant energy gap is taken as a first approximation. In general, the solar cell is illuminated by the sun and the atmosphere.

Here ϕ_{in} denotes the incoming hemispherical irradiance of the two contributions. The second term ϕ_{em} refers to the luminescence flux emitted by the solar cell as required by the detailed balance between absorption and emission of photons. It is given by the generalised Planck's law [35], as long as the temperature and the quasi-Fermi level splitting is constant over the thickness of the cell

$$\phi_{em}(E,T,V) = \frac{1}{4\pi^2\hbar^3c^2}\frac{E^3}{exp[(E-qV)/kT]-1} \tag{2}$$

where $\hbar$ is the reduced Planck's constant, c the speed of light. The equation (2) describes an hemispherical emission of photons restricted to the front side [36], by means of a perfect reflector on the rear. The maximum energy conversion efficiency given by this approach is 33,7% for a band gap energy of 1.34 eV under standard test conditions. This value is slightly different from that obtained with the original Shockley-Queisser model (i.e. an ideal diode model) because we do not assume thermal equilibrium with a surrounding blackbody radiation and do not approximate carrier statistics by the Maxwell-Boltzmann distribution. This makes our model more general and valid in a wider range of temperature.

The cell temperature T is calculated using the balance between heat sources (l.h.s) and heat sinks (r.h.s)

$$P_{in}^{bb} + P_{in}^{th} = P_{em}^{bb} + P_{em}^{th} + P_{elec} + P_{con} \tag{3}$$

Convection is described by the P_{con} term. It acts as a heat sink as long as the device temperature T lies above the ambient temperature T_a

$$P_{con} = h(T - T_a) \tag{4}$$

with h the convective heat transfer coefficient [37] of the front side, in W.m^{-2}.K^{-1}. In equation 3, we consider that the heat transfer is restricted to the front side only. The extended model presented in the appendix makes it possible to also take into account convection and radiation on the back and sides of the device.

The P_{in}^{bb} term denotes the power density absorbed by band-to-band transitions

$$P_{in}^{bb} = \int_{E_g}^{\infty} \phi_{in}(E)dE \tag{5}$$

Part of this energy is converted into electricity P_{elec}, according to the previously established equation, while another part P_{em}^{bb} is emitted back to the surrounding due to luminescence

$$P_{em}^{bb} = \int_{E_g}^{\infty} \phi_{em}(E,T,V)dE \tag{6}$$

The device is also required to absorb thermal radiation from the atmosphere, mainly in the mid-infrared and far-infrared range of the spectrum. We assume that these absorptions occur only for photons with energies below the band gap energy, as required by an ideal solar cell with perfect band-to-band absorption. Hence, we allow a non-zero thermal absorptance $\alpha(E)$ only for energies $E < E_g$

$$P_{in}^{th} = \int_{0}^{E_g} \alpha(E)\phi_{in}(E)dE \tag{7}$$

Accordingly to Kirchhoff's law, the device also emits thermal radiation with a thermal emissivity ϵ equal to its thermal absorptance

$$P_{em}^{th} = \int_{0}^{E_g} \epsilon(E)\phi_{em}(E,T,0)dE \tag{8}$$

Thermal emission is always present in solar cells due to free carriers and lattice. Even though it might be weak without optimisation and lead to poor radiative cooling properties, one can shape the emissivity profile by photonic microstructures or by adding a radiative cooling layer as depicted in figure 2. In the latter case our model remains valid as long as there is a perfect thermal coupling between the solar cell and the cooling layer.

To summarise, the proposed modelling allows us assess both the electrical output power and the cell temperature at the MPP, as a function of the environmental conditions and the fundamental parameters involved in the thermoelectric modelling. Hence, it is very general and does not require any empirical parameters unlike other approaches, such as a temperature sensitivity coefficient [24]. This makes it a powerful tool to explain and predict the influence of RSC on a wide range of systems. In particular, it allows to predict the temperature reduction due to enhanced RSC, according to a change in the thermal emissivity profile $\epsilon(\lambda)$.

2.2 Thermal emissivity model

Changing the emissivity in the thermal wavelength range (i.e. for energies smaller than E_g) has a two-fold influence on thermal management. First, parasitic solar absorption can occur below $\sim$4 μm if the thermal emissivity is high in this range. At longer wavelengths, the emissivity profile influences the balance between emission and absorption of atmospheric radiation. To study the impact of these two phenomena, we introduce an appropriate step-model for the emissivity ϵ, as depicted in figure 2. For convenience, it is represented as a function of wavelength rather than energy

$$\epsilon(\lambda) = \begin{cases} \epsilon_1 & \text{for } \lambda_g < \lambda \leq \lambda_1 \\ \epsilon_2 & \text{for } \lambda_1 < \lambda \leq \lambda_2 \\ 0 & \text{elsewhere} \end{cases} \tag{9}$$

with λ_g being the threshold wavelength associated with the band gap energy E_g. The solar spectrum has almost no overlap with the thermal emission and absorption spectrum (inset of figure 2). By setting λ_1 to 4 μm it is thus possible to decouple the contribution of parasitic solar absorption (value of ϵ_1) and radiative heat exchange with the atmosphere (value of ϵ_2). When taking λ_1=4 μm and $\lambda_2 \to \infty$, the broadband profile is retrieved. When now setting λ_1=8 μm and λ_2=13 μm together with ϵ_1=0 and ϵ_2=1, the selective profile is retrieved. It should be noted that the radiative heat exchange must be calculated well beyond 20 μm as, for example, a blackbody at 25 °C emits more than 25% of its energy beyond this wavelength. In this study, λ_2 was therefore set to 100 μm. Sensitivity to this threshold wavelength is studied in more detail in section 3.

2.3 Reference environmental conditions

Choosing a relevant set of environmental conditions is of significance to assess the potential of a cooling strategy. Indeed, the predicted temperature reduction attributed to radiative sky cooling greatly changes according to the level of solar and atmospheric irradiance, ambient temperature, and wind speed. Defining reference climatic conditions is also essential to compare the potential between technologies.

To show the potential in terms of temperature reduction and power enhancement, we require for these conditions to be favourable to RSC while remaining close to real operating conditions. To follow the path of the photovoltaic community and respect these constraints, we choose the standard ASTM G-173-03 spectrum for solar irradiance. Accordingly, the atmospheric hemispherical irradiance is given by the US standard atmosphere and an ambient temperature of 15 °C (figure 1). In the 4-20 μm range, data for the atmosphere is taken from X. Yu and C. Chen [16]. Beyond 20 μm, we assume an opaque atmosphere. The convection level is set to h = 5 W.m^{-2}.K^{-1} (natural convection [38]) in the first place, i.e. when radiative cooling is of primary importance. The influence of variable convection, solar irradiance, and transparency of the atmosphere is discussed elsewhere in the results section.

3 Results and discussion

In this section, we first compare the operating temperature and the electrical output power provided by the selective and the broadband emissivity profiles in different scenarios, in order to determine the ideal profile for single-junction cells. Then, we also allow for parasitic sub-band gap absorption. Using the step-model emissivity, we assess the cooling potential for Si, GaAs, and perovskite based devices according to their initial thermal emissivity profile. Lastly, we study the sensitivity of this potential to major effects that are generally present in real devices (i.e with non-ideal electrical and optical properties, or rear/lateral heat transfer). As a case study, we consider Si-based devices.

3.1 Broadband against selective thermal emission

In order to asses the potential of radiative sky cooling for solar cells it is first necessary to know which thermal emissivity profile provides the best benefit. As mentioned in the introduction, there are two competitors for the latter: the broadband profile and the selective profile. Whether one or the other is the ideal thermal emissivity is not trivial because solar cells are required to operate in a wide range of climatic conditions and may exhibit a different thermoelectric behaviour. As a starting point, we investigate the influence of the cell band gap under the reference climatic conditions defined in the method section. We then study the effect of solar and atmospheric irradiance on the cell temperature and electrical power output provided by both profiles.

Figure 3 depicts the cell temperature as a function of its energy band gap, for a selective and a broadband thermal emissivity. Under the reference spectral conditions chosen here, it can be seen that the broadband profile allows lower operating temperatures than the selective profile as long as the band gap is smaller than $\sim$2.3 eV. This energy gap also roughly coincides with the limit between the above-ambient ($T > T_a$) and the below-ambient ($T < T_a$) temperature

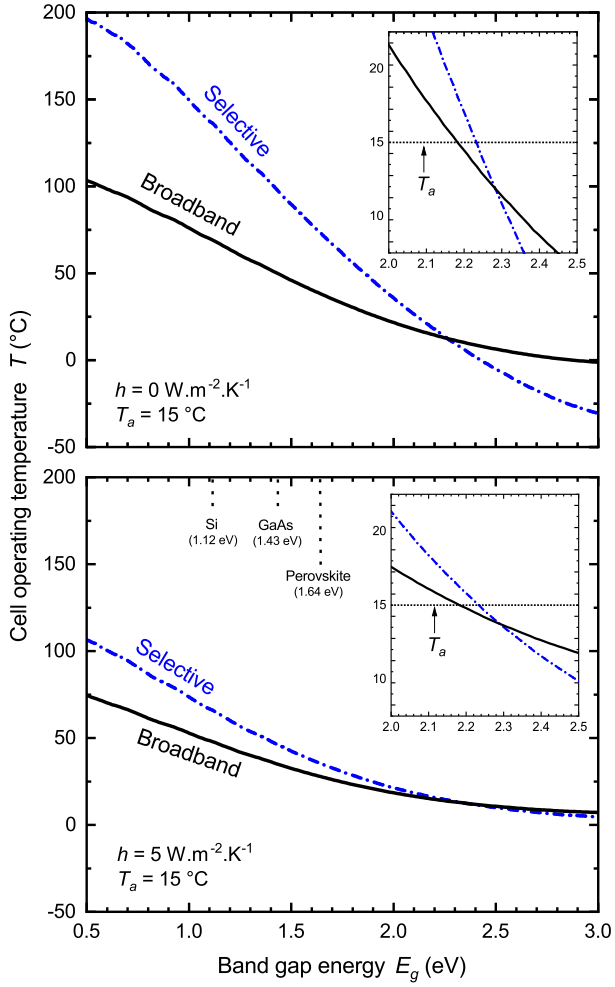

Figure 3: Operating temperature for a selective and a broadband thermal emissivity profile as a function of the cell energy band gap. The temperature is calculated without convection (upper graph) and with a natural convection level (lower graph). The energy gaps at 25 °C used in this work, for Si [39], GaAs [39], and perovskite [40] cells are also represented.

regime for both emissivity profiles, as shown in insets. This is due to the fact that, when the cell temperature is above ambient, the broadband profile always offers a higher net radiative power $P_{em}^{th} - P_{in}^{th}$ than the selective profile, as in this case the difference between the heat emitted by thermal radiation and the heat absorbed from the atmosphere is positive regardless of the wavelength (upper graph of figure 1). On the other hand, the selective profile restricts the radiative exchange to wavelengths inside the 8-13 μm atmospheric window and therefore provides a higher net radiative power $P_{em}^{th} - P_{in}^{th}$ in the below-ambient temperature regime (lower graph of figure 1). Thus, selective emission is no longer of interest when the temperature is restricted above ambient due, for example, to heat generated by solar absorption. It is also noticeable to see from the inset of figure 3 that the broadband profile allows lower temperatures slightly below ambient as it takes advantage of the other regions of transparency in the atmospheric spectrum.

Convective heat transfer has a two-fold impact on the results of figure 3. First, it reduces the temperature difference between the selective and the broadband profile. Whereas, without convection (upper graph), the broadband profile allows a temperature 67 °C lower for a 1.12 eV band gap (Si), the decrease is only 18 °C when natural convection is present (lower graph). The difference is greater for higher band gaps: for GaAs and perovskite based cells it goes from 48 °C to 11 °C, and 35 °C to 8 °C, respectively. More importantly, the difference is strongly reduced for cells that operate below the ambient temperature. For example, for a band gap energy E_g = 3.0 eV, the difference goes from 31 °C without convection to only 2 °C with it. Second, the reader's attention is drawn to the fact that convection acts differently in the above-ambient and below-ambient temperature regime. In the first case, convection acts as a heat

sink and therefore allows lower temperatures. In the second case, convection becomes a heat source which limits the temperature reduction achievable with RSC.

It should also be noted that the level of convection h slightly changes the band gap energy where the selective profile overcomes the broadband profile, but does not affect the band gap where the transition to the below-ambient regime occurs. This is due to the fact that the convective flow vanishes when the cell temperature tends to the ambient temperature.

Thus, a selective profile is only appropriate for cells with a large band gap energy ($E_g \geq 2.3$ eV) and require the suppression of convection. Indeed this combination would allow cell temperatures well below the ambient temperature, even under strong solar irradiance as considered here. As terrestrial solar cells generally have much smaller band gaps, the broadband profile appears to be more profitable and convection should not be suppressed. However, since PV devices can be subjected to a wide range of environmental conditions, especially variable solar and atmospheric irradiance, it is important to gain more insights on those.

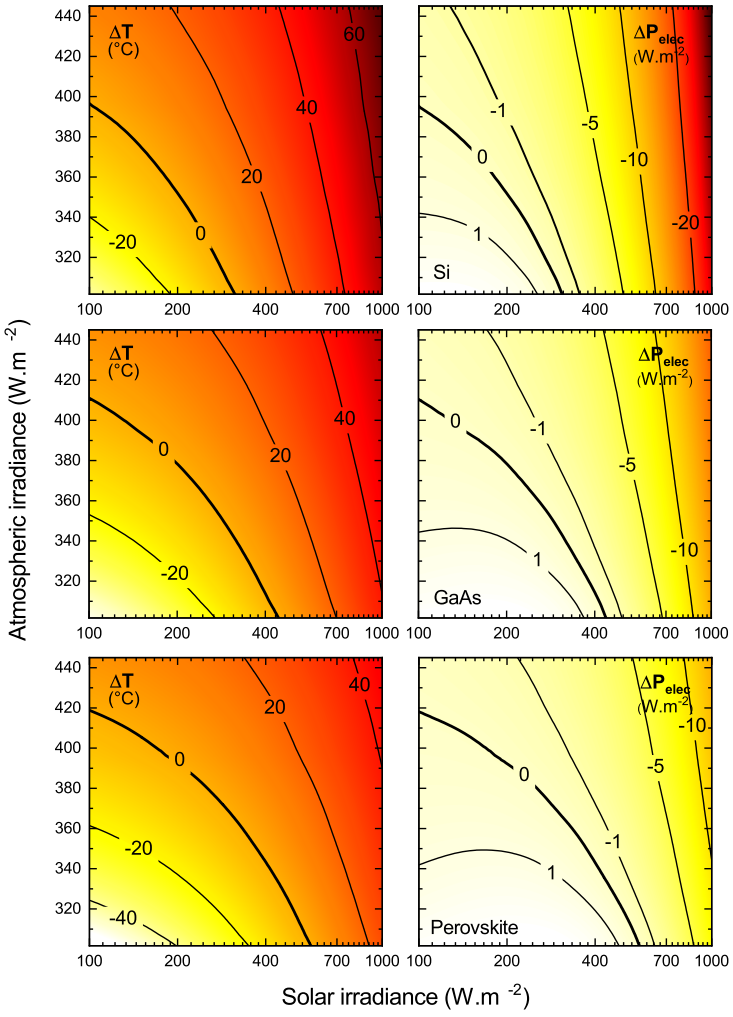

Figure 4: Difference in performance (operating temperature and output power) between a selective and a broadband profile as a function of solar and atmospheric irradiance levels. The thick solid line shows the conditions for which the two profiles have the same cooling properties. The results are calculated without convection, for Si (upper graphs), GaAs (middle graphs), and perovskite (lower graphs) cells. The solar spectrum, modelled by a 5527 °C (5800 K) blackbody, is normalised to give the desired intensity. The atmospheric irradiance is modelled by a blackbody at T_a = 25 °C outside the 8-13 μm transparency window, and by a greybody within this range. The irradiance in the 8-13 μm window is modified by changing the atmospheric emissivity between 0 (perfectly transparent atmosphere) and 1 (opaque atmosphere), according to the model proposed by Granqvist and Hjortsberg [14].

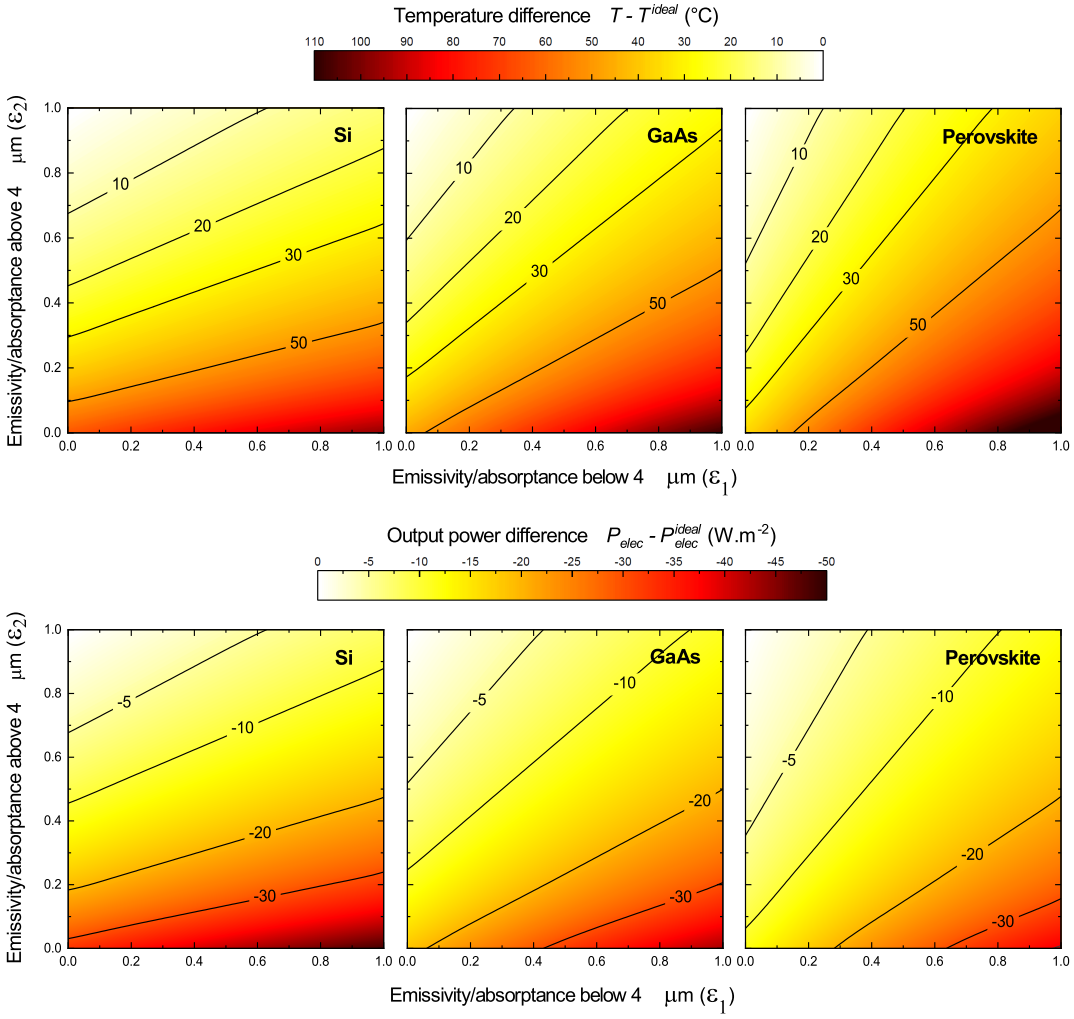

Figure 5: Difference in performance (temperature on the upper part and output power on the lower part) between an ideal broadband profile and an emissivity profile that includes parasitic solar absorption below 4 μm ($\epsilon_1 \neq 0$) and less thermal emission beyond 4 um ($\epsilon_2 \neq 1$). The results are given for Si, GaAs and perovskite cells with a natural convection level (h = 5 W.m^{-2}.K^{-1}). This illustrate the potential of enhanced radiative sky cooling as a function of the initial emissivity profile. The solid lines represents the isothermal (left) and isopower (right) curves.

To highlight their influence, figure 4 shows the difference in temperature ΔT and electrical power output ΔP_{elec} between cells with a selective emissivity profile and cells with the broadband profile. For $\Delta T > 0$ and $\Delta P_{elec} < 0$, the broadband profile performs better. The differences are computed as a function of solar and atmospheric irradiance. The atmospheric irradiance is mainly related to the transparency of the atmosphere in the 8-13 μm range: the higher the transparency, the lower the total atmospheric irradiance. As shown on the vertical axis of figure 4, it can vary by about 140 W.m^{-2} between a perfectly transparent atmosphere in 8-13 μm range (lower bound of the vertical axis) and an opaque atmosphere (upper bound of the vertical axis), when the ambient temperature is 25 °C. This order of magnitude is in good agreement with pyrgeometer measurements in warm seasons [41]. The solar irradiance varies according to the location, the season, and the time of the day, reaching up to $\sim$1000 W.m^{-2} on clear days, even in mid-latitude sites on summer days[42]. It also depends upon the atmospheric transparency, but the relationship between the two is not straightforward. For example cloud cover, which is known to opacify the atmospheric window [31], can under certain conditions increase solar irradiance [43]. Thus, we consider all possible combinations but we ask the reader to bear this in mind when looking at results of figure 4. Moreover, we consider a scenario where the ambient temperature is high (T_a = 25 °C) and where convective heat transfer is suppressed, i.e. a case rather favourable to the selective profile.

Even in this scenario, the benefit provided by the selective profile appears to be small compared to that provided by the broadband profile. It can be seen that the broadband profile allows better performance as soon as the solar irradiance exceeds 310 W.m^{-2} for Si, 430 W.m^{-2} for GaAs, and 570 W.m^{-2} for perovskite cells, even if the atmosphere is completely transparent in the 8-13 μm range. This threshold is too low to benefit the selective profile. Under 1000 W.m^{-2} solar irradiance, the latter would lead to temperatures up to 40-60 °C higher than the broadband profile. This would accelerate degradation and lead to a significant peak power loss: up to 30 W.m^{-2} for Si, 20 W.m^{-2} for GaAs, and 15 W.m^{-2} for perovskite. This loss is high compared to the gain of 1-2 W.m^{-2} allowed by the selective profile under lower illumination. Obviously, the more opaque the atmosphere is, the more the threshold illumination decreases. However, it is important to notice that this behaviour is in favor of the broadband profile. Especially, if solar irradiance is low due to cloud cover, then the atmospheric irradiance will generally be high [31]. One could argue that the threshold illumination is rather high in certain situations, e.g. for mid-latitude regions in winter or autumn, but the ambient temperature is then generally much lower which causes the threshold illumination to further drop. For example, additional simulation shows that the threshold for Si is only $\sim$140 W.m^{-2} when the ambient temperature is 15 °C and the atmosphere is entirely transparent between 8 μm and 13 μm.

This shows that the broadband profile is the ideal emissivity for single-junction cells operating in terrestrial conditions, as it significantly lowers their temperature and increases their electrical power output in most scenarios. If we allow for convection, we expect even better performance for the broadband profile.

3.2 Cooling potential of ideal single-junction cells

We demonstrated that the broadband profile is the ideal one. This allows us to assess the potential of RSC. Once again, this potential depends on environmental conditions, and we therefore consider the reference conditions to begin with. More importantly, the potential depends on the initial thermal emissivity profile, that is the emissivity for wavelengths λ greater than λ_g. We use the previously introduced step-model to study the influence of the latter by decoupling the effect of sub-band gap solar absorption (emissivity ϵ_1 below 4 μm) and radiative heat exchange with the atmosphere (emissivity ϵ_2 above 4 μm)

Figure 5 shows the heating and the electrical power loss attributable to these two phenomena with respect to the ideal emissivity profile, i.e ϵ_1 = 0 and ϵ_2 = 1 (top left corner of the graphs), for Si, GaAs, and perovskite cells. In all cases, the importance of tailoring thermal emission can be stressed. A total suppression of thermal emission together with strong parasitic solar absorption (ϵ_1 = 1, ϵ_2 = 0) would lead to a temperature increase of more than 100 °C and a power loss of 50 W.m^{-2}. This figure also shows that a reduction of nearly 10 °C is achievable thanks to the broadband profile even if the device has already a reasonably good emissivity profile ($\epsilon_1 \sim 0.2$ and $\epsilon_2 \sim 0.8$). This would increase the peak power by almost 5 W.m^{-2} even for ideal single-junction cells as considered here ($\sim$ +0.5 % absolute energy conversion efficiency). As explained in section 3.3, a higher potential is expected for non-ideal cells operating far from the radiative limit due to their higher operating temperatures and temperature sensitivity coefficients.

Figure 5 also highlights different trends for the three technologies. For silicon cells, increasing the emissivity above 4 μm appears to be the main optical lever for cooling: as a rule of thumb, a 10% increase above 4 μm is equivalent to a 20% decrease in emissivity below 4 μm. For GaAs and perovskite cells, the temperature decrease is more sensitive to parasitic solar absorption because of their higher band gap.

The cooling potential also depends on how a real emissivity profile could be tailored to fit the emission thresholds of the ideal case, namely the values of λ_1 and λ_2. Figure 6 describes the temperature difference $T - T^{ideal}$ between a cell with a cell with a variable threshold wavelength λ_1 and a cell with the ideal broadband profile (λ_1 = 4 μm and λ_2 = 100 μm), for different values of λ_2. Here, ϵ_1 and ϵ_2 are kept to 0 and 1, respectively. The graph shows clearly a minimum for λ_1 = 4 μm. In order to keep a temperature difference of less than 1 °C with this minimum (the ideal profile), it is sufficient to have λ_1 between $\sim$2.5 and $\sim$4.5 μm. Additionally, λ_2 should be greater than 40 μm. Increasing the emission between 40 μm and 60 μm only brings an additional temperature reduction of $\sim$0.3 °C.

3.3 Towards real devices: influence of non-ideal cell properties and back-side heat transfer

The results of sections 3.1 and 3.2 can be used as a fundamental basis for understanding and optimising radiative sky cooling of single-junction PV devices. In particular, they provide an order of magnitude of the potential of this strategy for three common technologies. However, the results are quantitatively accurate for devices that meet the assumptions of the thermoelectric modelling. In this part, we address the effect of first-order phenomenom that may occur in real devices. First, we investigate independently non-ideal cell properties. These are: 1) band gap temperature dependence; 2) non-radiative recombination; 3) imperfect band-to-band absorption. Then, we study the influence of additional heat transfers at the back and sides of the PV device. Si-based devices with an ideal broadband emissivity are considered here as a case study.

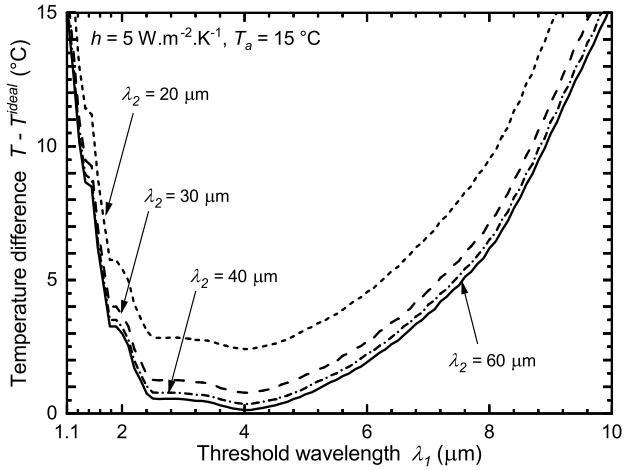

Figure 6: Temperature increase of a Si cell due to a non-ideal thermal emissivity profile: threshold wavelength for suppression of parasitic solar absorption λ_1 different from 4 μm, thermal emission restricted to a wavelength λ_2 below 100 μm. The reference spectral conditions are used.

The temperature variation attributable to non-ideal cell properties is pictured in Figure 7. This graph shows the temperature difference $T - T_{ref}$ between a cell with (Cases A, B, and C) or without these effects (Reference Case, i.e. $T = T_{ref}$), as well as the various heat sinks and sources. Case D shows the temperature difference when all the effects are considered together.

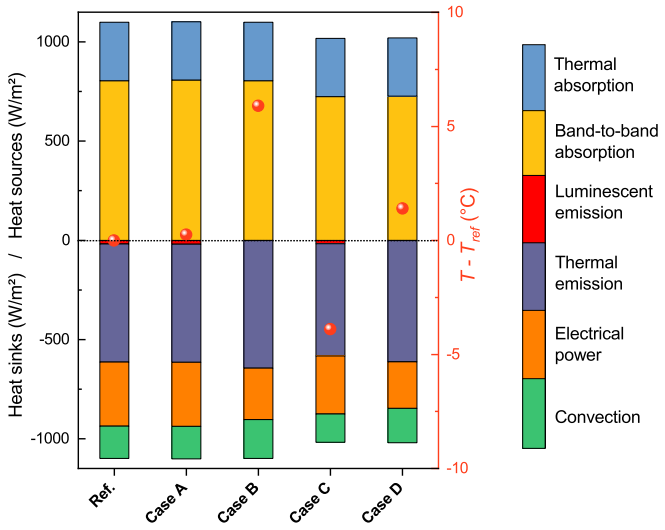

Figure 7: Influence on relative operating temperature $T - T_{ref}$ (red dots) and heat flows attributable to different first-order effects present in a real Si solar cell. The reference case ($T = T_{ref}$) shows the different heat sources and heat sinks for an ideal cell described by the model presented in the methods section. Case A shows the effect of the temperature dependence of the band gap. Case B shows the effect of non-radiative recombination (Q_e^{lum} = 1.6%, the radiative efficiency of the highest performing Si cell produced so far [44]) and case C the effect of non-ideal solar absorption (α_{bb} = 90%, representative of a 22% efficient PERC solar cell [45]). Case D results in the addition of these three phenomena. In each case, a broadband profile together with the reference environmental conditions (h = 5 W.m^{-2}.K^{-1}, T$_a$ = 15 °C) were chosen.

In a first step, the constant band gap energy is replaced by a temperature-dependent energy gap (Case A) for crystalline silicon [39]. As expected, the temperature is increased but the difference is rather small (+ 0.3 °C) compared to the other effects.

Second, we introduce the external luminescence efficiency Q_e^{lum} to take non-radiative recombination into account. This quantity is defined as the proportion of total dark current that leads to radiative emission from the cell (cf. Appendix). As can be seen from figure 7, the temperature of a state-of-the-art Si cell with a high Q_e^{lum} value (Case B) is already 6 °C higher than the temperature predicted for a cell operating within the radiative limit (Q_e^{lum} = 100 %, reference case). This is because non-radiative recombination reduce the operating voltage of the cell [2, 46]. Therefore, the electrical power extracted is also reduced and the heat extracted by luminescence becomes negligible compared to other heat sinks.

Next, the absorbed fraction of photons which carry energies higher than the band gap, α_{bb} (i.e. the band-to-band absorption coefficient), is changed to a realistic value (Case D). At 25 °C, a perfect solar absorption (α_{bb} = 1.0) leads to a short-circuit current of approx. 44 mA.cm^{-2}. State-of-the-art cells [44] reach currents of 42.6 mA.cm^{-2} whereas industrial cells [45] reach currents close to 40 mA.cm^{-2}, which corresponds to an already good absorption coefficient $\alpha_{bb} \sim 0.9$. In this case, the temperature is significantly reduced by 4 °C.

Altogether (Case D), however, the temperature is higher than for an ideal cell. As lower quality cells generally have comparable solar absorption due to anti-reflection coatings and pyramid texturing but higher non-radiative recombination rates, higher temperatures are expected for these cells. In addition, effects such as resistance loss or charge carrier collection loss [25], not considered here, should further reduce the energy conversion efficiency and thus increase the cell temperature. Therefore, we expect an even higher absolute temperature reduction achievable with RSC for most solar cells. Non-radiative recombination are also known to increase the temperature sensitivity coefficient [34]. For the same temperature reduction, this would lead to a higher relative electrical power enhancement for cell operating far from the radiative limit.

Finally, we analyse the influence of heat transfer that are present on the back and sides of the device. As a first approximation, this effect can be described by introducing an effective heat exchange coefficient $h*$ that accounts for both natural convection and thermal radiation [37] (see the appendix for further details), because the radiative exchange of surfaces that do not face the sky is also limited by the ambient temperature. In essence, an increase in convection or radiation at the back and/or sides has the same effect as an increase in front-side convection: a lower device temperature in the above-ambient regime, and therefore a lower cooling potential of RSC. This also indicates that the broadband profile remains the ideal thermal emissivity, even in presence of these additional heat transfers, because the below-ambient regime would be more difficult to achieve.

Figure 8 shows the reduction in cooling potential as a function of h^* for a Si cell. The graph represents the temperature decrease that can be achieved by switching from an already good emissivity profile (ϵ_1 = 0.3 and ϵ_2 = 0.8) to the ideal profile (a gain of about 10 °C is expected if we allow only heat transfers at the front, i.e. for h^* = 0). Although the potential decreases when the rear side heat transfer increases, it remains above 3 °C even for h^* = 15 W.m^{-2}.K^{-1}. This difference is almost the same when considering a thick device with lateral heat transfers (difference between the lower limits of the curves in figure 8). More importantly, this reduction remains of the same order of magnitude than an improvement in h^* above $\sim$10 W.m^{-2}.K^{-1}. In this sense, RSC appears to be a complementary lever to other passive cooling strategies even for thick systems.

4 Conclusions

In summary, a fundamental modelling framework was presented to study the influence of radiative sky cooling on the thermoelectic behaviour of single-junction solar cells. Thanks to this model, we demonstrate that a broadband emissivity profile provides the best performance for radiative sky cooling of single-junction devices operating under terrestrial conditions. Compared to a selective emissivity, the broadband profile allows much lower temperatures (up to 60 °C lower with a 1000 W.m^{-2} solar illumination) as long as the solar illumination exceeds $\sim$300 W.m^{-2} for a solar absorber with a 1.12 eV band gap (Si), and $\sim$500 W.m^{-2} for an absorber with a 1.64 eV band gap (perovskite). This allows for a significantly higher electrical power output than a selective emissivity (up to 30 W.m^{-2} with a 1000 W.m^{-2} illumination).

For near-ideal cells (i.e. operating close to the radiative limit and with perfect band-to-band absorption), our simulations show that an improvement in RSC can easily reduce the cell temperature by 10 °C. This would increase their power output by more than 5 W.m^{-2}. For Si-based devices with high non-radiative recombination, our model predicts an even higher temperature reduction. This cooling potential appears to be unchanged as long as the thermal emissivity profile fits the broadband profile up to 40 μm, meaning that optimising the emissivity beyond this limit will result in a temperature decrease of less than 0.5 °C. The potential is reduced when lateral and rear side heat transfer is important and/or for thick devices, as they already operate in a lower temperature regime. However, the radiative sky cooling strategy remains important to cool them down further. Even in the worst scenario (a thick device with initially good thermal management on the front and the rear), a broadband profile can further reduce the temperature by almost 3 °C.

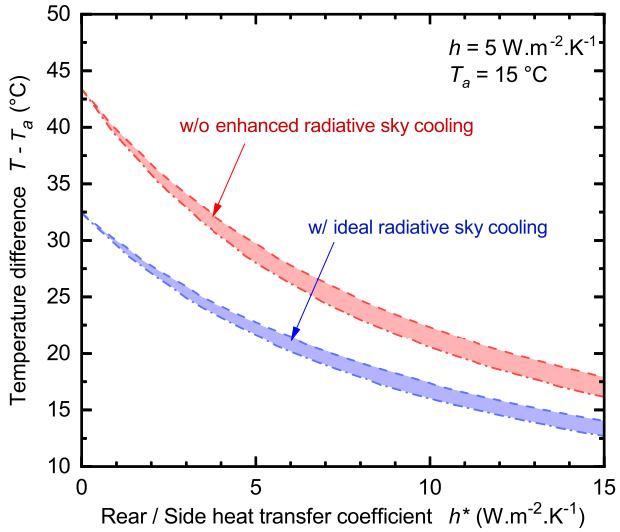

Figure 8: Influence of heat transfers (conductive and/or radiative) present on the back and the sides of the PV device. The dashed lines represent the temperature of a flat device (negligible lateral heat transfers) and the dot-dashed lines the temperature of a thick device (i.e. a Si cell encapsulated into a standard module : 156 mm^2 x 5 mm (surface x depth). Both are calculated for a system without enhanced radiative sky cooling (red area) and with an ideal broadband profile (blue area). The case without improved sky cooling already shows good optical properties on the front side (30% of parasitic solar absorption together with a 80% thermal emissivity above 4 μm). Results are calculated for a device based on silicon, operating under the reference environmental conditions.

Parasitic sub-band gap solar absorption play an important role in thermal management of single-junction cells. For Si cells, we show that a 20% reduction in parasitic absorption produces roughly the same effect as a 10% increase in emissivity above 4 μm. For GaAs and perovskite cells, the effect is even more pronounced. In order to predict in detail the cooling potential of a device according to its initial thermal emissivity, we have developed graphs accounting for both sub-band gap solar absorption below 4 μm and thermal emission above 4 μm. These can be used as a guide for device optimisation or for further simulation-based studies. Our model could also easily be extended to study the fundamental thermoelectric behaviour of other PV technologies, such a multi-junction solar cells.

5 Appendix

To gain insights on additional phenomena in real devices, one can extend the detailed-balance model to a more general situation by the use of external parameters [46]. First, if we allow for non-radiative recombination to happen, we include the external luminescence efficiency Q_e^{lum}, which is defined as [2]

$$Q_e^{lum} = \frac{J_{gen}^{bb} - J_{rec}^{rad}(V)}{J_{gen}^{bb} - J_{rec}^{rad}(V) + J_{gen}^{non-rad} - J_{rec}^{non-rad}(V)} \tag{10}$$

with J_{gen}^{bb} being the current density generated under dark conditions by surrounding blackbody radiation in thermal equilibrium with the cell

$$J_{gen}^{bb} = q \int_{E_g}^{\infty} \phi_{em}(E,T,0) \frac{dE}{E} \tag{11}$$

and $J_{rec}^{rad}(V)$ the current density loss due to radiative recombination

$$J_{rec}^{rad}(V) = q \int_{E_g}^{\infty} \phi_{em}(E,T,V) \frac{dE}{E} \tag{12}$$

Quantities $J_{gen}^{non-rad}$ and $J_{rec}^{non-rad}(V)$ refer respectively to the generation and recombination current due to non-radiative effects. The total current density J under illumination can be written as

$$\begin{aligned} J &= J_{in} - J_{gen}^{bb} + \frac{1}{Q_e^{lum}}(J_{gen}^{bb} - J_{rec}^{rad}(V)) \\ &\simeq J_{in} + \frac{J_{gen}^{bb}}{Q_e^{lum}}(1 - exp(\frac{qV}{kT})) \end{aligned} \tag{13}$$

where J_{in} is the current density generated by absorption of photons from the sun and the surrounding atmosphere

$$J_{in} = q\int_{E_g}^{\infty} \phi_{in}(E)\frac{dE}{E} \tag{14}$$

The electrical power P_{elec} then rewrites as

$$P'_{elec} = qV\int_{E_g}^{\infty} (\phi_{in} - \phi_{em}(T,0) - \frac{\phi_{em}(T,V) - \phi_{em}(T,0)}{Q_e^{lum}})\frac{dE}{E} \tag{15}$$

Within the limit where the approximation of equation 13 is valid (the typical one diode model with non-radiative recombination), we see that the quantity Q_e^{lum} corresponds to the proportion of total dark current that leads to radiative emission from the cell [46].

Second, we switch from the ideal band-to-band absorptance equal to the step function $H(E - E_g)$, to a more realistic situation where band-to-band absorption is less efficient and the temperature dependence of the band gap energy of the material is taken into account as $\alpha_{bb}H(E - E_g(T))$, with α_{bb} between 0 and 1

$$P''_{elec} = qV\alpha_{bb}\int_{E_g(T)}^{\infty} (\phi_{in} - \phi_{em}(T,0) - \frac{\phi_{em}(T,V) - \phi_{em}(T,0)}{Q_e^{lum}})\frac{dE}{E} \tag{16}$$

The ideal expression (equation 1) is retrieved by setting α_{bb} = 1, Q_e^{lum} = 1 and by ignoring the temperature dependance of the band gap. As seen in table 1, this improved detailed-balance model is sufficient to describe the open-circuit voltage V_{oc} of a state-of-the-art Si solar cell with only $\sim$2% relative error.

Table 1: Comparison between electrical parameters obtained with our detailed-balance model (ideal and extended) and electrical parameters of a real Si cell. The value of Q_e^{lum} was taken from ref. [44], and the value of α_{bb} was chosen to fit the short-circuit density jsc.

Model	E_g (eV)	α_{bb}	Q_e^{lum}	J_{sc} (mA.cm^{-2})	V_{oc} (V)	efficiency (%)
ideal	1.1	1.0	1.0	44.22	0.860	33.0
extended	1.1	0.965	0.016	42.65	0.754	27.4
exp. [44]	1.1	/	0.016	42.65	0.738	26.7

To take the heat exchange on the back and sides of the device into account, we add two parameters to the heat balance. First, a combined heat transfer coefficient h^* is introduced for these surfaces to account for both convection and radiation. As a first approximation, the latter effect is limited by the ambient temperature T_a because the rear/sides do not face the sky, so that the net heat flux at the rear/sides $P_{r/s}$ is [37]

$$P_{r/s} = S_{r/s}h^*(T - T_a) \tag{17}$$

with $S_{r/s}$ the sum of the rear and side surfaces of the device. The combined heat transfer coefficient h^* writes as

$$h^* = h_{r/s} + \epsilon_{r/s}\sigma(T + T_a)(T^2 + T_a^2) \tag{18}$$

$h_{r/s}$ being the convective heat transfer at the rear/sides, $\epsilon_{r/s}$ the emissivity, σ the Stefan-Boltzmann constant. For a perfectly emitting surface ($\epsilon_{r/s}$ = 1), the second term of equation 18 is only 6 W.m^{-2}.K^{-1} when $T = T_a$ = 25 °C. When taking T = 100 °C and T_a = 25 °C, it remains less than 10 W.m^{-2}.K^{-1} so that the h^* is in the range 5-15 W.m^{-2}.K^{-1} for natural convection. Finally, a geometric factor s is introduced. It represents the ratio between the front surface and the total surface, so that the heat balance (equation 3) simply rewrites as

$$P_{in}^{bb} + P_{in}^{th} = P_{em}^{bb} + P_{em}^{th} + P_{elec} + P_{con} + (s^{-1} - 1)h^*(T - T_a) \tag{19}$$

From equation 19, we see that this additional heat transfer acts in the same way than front convection (equation 4).

References

[1] Martin A. Green, Ewan D. Dunlop, Jochen Hohl-Ebinger, Masahiro Yoshita, Nikos Kopidakis, and Anita W.Y. Ho-Baillie. Solar cell efficiency tables (Version 55). *Progress in Photovoltaics: Research and Applications*, 28(1):3–15, 2020.

[2] William Shockley and Hans J. Queisser. Detailed balance limit of efficiency of p-n junction solar cells. *Journal of Applied Physics*, 32(3):510–519, mar 1961.

[3] Armin Richter, Martin Hermle, and Stefan W. Glunz. Reassessment of the limiting efficiency for crystalline silicon solar cells. *IEEE Journal of Photovoltaics*, 3(4):1184–1191, 2013.

[4] Lucas Weiss, Mohamed Amara, and Christophe Ménézo. Impact of radiative-heat transfer on photovoltaic module temperature. *Progress in Photovoltaics: Research and Applications*, 24(1):12–27, jan 2016.

[5] E. Skoplaki and J. A. Palyvos. On the temperature dependence of photovoltaic module electrical performance: A review of efficiency/power correlations. *Solar Energy*, 83(5):614–624, 2009.

[6] D.H. Otth and R.G. Ross. Assessing photovoltaic module degradation and lifetime from long term environmental tests. In *29th Institute of Environmental Sciences, Annual Technical Meeting*, pages 121–126, 1983.

[7] A. W. Kandeal, Amrit Kumar Thakur, M. R. Elkadeem, Mahmoud F. Elmorshedy, Zia Ullah, Ravishankar Sathyamurthy, and Swellam W. Sharshir. Photovoltaics performance improvement using different cooling methodologies: A state-of-art review. *Journal of Cleaner Production*, 273:122772, 2020.

[8] S. Nižetić, E. Giama, and A. M. Papadopoulos. Comprehensive analysis and general economic-environmental evaluation of cooling techniques for photovoltaic panels, Part II: Active cooling techniques. *Energy Conversion and Management*, 155(October 2017):301–323, 2018.

[9] S. Nižetić, A. M. Papadopoulos, and E. Giama. Comprehensive analysis and general economic-environmental evaluation of cooling techniques for photovoltaic panels, Part I: Passive cooling techniques. *Energy Conversion and Management*, 149:334–354, 2017.

[10] A. Shukla, Karunesh Kant, Atul Sharma, and Pascal Henry Biwole. Cooling methodologies of photovoltaic module for enhancing electrical efficiency: A review. *Solar Energy Materials and Solar Cells*, 160(July 2016):275–286, 2017.

[11] Dengfeng Du, Jo Darkwa, and Georgios Kokogiannakis. Thermal management systems for Photovoltaics (PV) installations: A critical review. *Solar Energy*, 97:238–254, 2013.

[12] Félix Trombe. Sur des grands abaissements de température obtenus par rayonnement du corps noir sur l'espace. *Comptes rendus de l'Académie des sciences*, 256:735–738, 1963.

[13] S. Catalanotti, V. Cuomo, G. Piro, D. Ruggi, V. Silvestrini, and G. Troise. The radiative cooling of selective surfaces. *Solar Energy*, 17(2):83–89, 1975.

[14] C. G. Granqvist and A. Hjortsberg. Radiative cooling to low temperatures: General considerations and application to selectively emitting SiO films. *Journal of Applied Physics*, 52(6):4205–4220, 1981.

[15] Zhen Chen, Linxiao Zhu, Aaswath Raman, and Shanhui Fan. Radiative cooling to deep sub-freezing temperatures through a 24-h day-night cycle. *Nature Communications*, 7:1–5, 2016.

[16] Xinxian Yu and Chun Chen. A simulation study for comparing the cooling performance of different daytime radiative cooling materials. *Solar Energy Materials and Solar Cells*, 209(January):110459, 2020.

[17] Linxiao Zhu, Aaswath Raman, Ken Xingze Wang, Marc Abou Anoma, and Shanhui Fan. Radiative cooling of solar cells. *Optica*, 1(1):32, 2014.

[18] Linxiao Zhu, Aaswath P. Raman, and Shanhui Fan. Radiative cooling of solar absorbers using a visibly transparent photonic crystal thermal blackbody. *Proceedings of the National Academy of Sciences of the United States of America*, 112(40):12282–12287, 2015.

[19] Linshuang Long, Yue Yang, and Liping Wang. Simultaneously enhanced solar absorption and radiative cooling with thin silica micro-grating coatings for silicon solar cells. *Solar Energy Materials and Solar Cells*, 197(April):19–24, 2019.

[20] Yidan An, Chunxiang Sheng, and Xiaofeng Li. Radiative cooling of solar cells: opto-electro-thermal physics and modeling. *Nanoscale*, 11:17073–17083, 2019.

[21] Taqiyyah S. Safi and Jeremy N. Munday. Improving photovoltaic performance through radiative cooling in both terrestrial and extraterrestrial environments. *Optics Express*, 23(19):A1120–A1128, 2015.

[22] A. R. Gentle and G. B. Smith. Is enhanced radiative cooling of solar cell modules worth pursuing? *Solar Energy Materials and Solar Cells*, 150:39–42, 2016.

[23] Wei Li, Yu Shi, Kaifeng Chen, Linxiao Zhu, and Shanhui Fan. A Comprehensive Photonic Approach for Solar Cell Cooling. *ACS Photonics*, 4(4):774–782, 2017.

[24] Xingshu Sun, Timothy J. Silverman, Zhiguang Zhou, Mohammad Ryyan Khan, Peter Bermel, and Muhammad Ashraful Alam. Optics-Based Approach to Thermal Management of Photovoltaics: Selective-Spectral and Radiative Cooling. *IEEE Journal of Photovoltaics*, 7(2):566–574, 2017.

[25] Romain Couderc, Mohamed Amara, and Mustapha Lemiti. In-Depth Analysis of Heat Generation in Silicon Solar Cells. *IEEE Journal of Photovoltaics*, 6(5):1123–1131, 2016.

[26] Benoit Guillo Lohan, Mohamed Amara, Anne Kaminski-Cachopo, and Mustapha Lemiti. Innovative experimental setup for thermal and electrical characterization of silicon solar cells under controlled environmental conditions. *Solar Energy Materials and Solar Cells*, 185(May):300–306, 2018.

[27] Malte R. Vogt, Hendrik Holst, Matthias Winter, Rolf Brendel, and Pietro P. Altermatt. Numerical Modeling of c-Si PV Modules by Coupling the Semiconductor with the Thermal Conduction, Convection and Radiation Equations. *Energy Procedia*, 77:215–224, 2015.

[28] Avinash Kumar and Amartya Chowdhury. Reassessment of different antireflection coatings for crystalline silicon solar cell in view of their passive radiative cooling properties. *Solar Energy*, 183(November 2018):410–418, 2019.

[29] Md Muntasir Hossain and Min Gu. Radiative cooling: Principles, progress, and potentials. *Advanced Science*, 3(7):1–10, 2016.

[30] Xingshu Sun, Yubo Sun, Zhiguang Zhou, Muhammad Ashraful Alam, and Peter Bermel. Radiative sky cooling: Fundamental physics, materials, structures, and applications. *Nanophotonics*, 6(5):997–1015, 2017.

[31] Dongliang Zhao, Ablimit Aili, Yao Zhai, Shaoyu Xu, Gang Tan, Xiaobo Yin, and Ronggui Yang. Radiative sky cooling: Fundamental principles, materials, and applications. *Applied Physics Reviews*, 6(2):021306, 2019.

[32] Gemini observatory, ir transmission spectra. `https://www.gemini.edu/observing/telescopes-and-sites/sites#Transmission`. Accessed: 2020-09-22.

[33] C. A. Gueymard, D. Myers, and K. Emery. Proposed reference irradiance spectra for solar energy systems testing. *Solar Energy*, 73(6):443–467, 2002.

[34] O. Dupré, R. Vaillon, and M. A. Green. Physics of the temperature coefficients of solar cells. *Solar Energy Materials and Solar Cells*, 140:92–100, 2015.

[35] P. Würfel and W. Ruppel. The chemical potential of luminescent radiation. *Journal of Luminescence*, 24-25(PART 2):925–928, 1981.

[36] Antonio Marti and Gerardo L Arafijo. Limiting efficiencies for photovoltaic energy conversion in multigap systems. *Solar Energy Materials and Solar Cells*, 43:203–222, 1996.

[37] Frank P. Incropera, David P. DeWitt, Theodore L. Bergman, and Adrienne S. Lavine. *Fundamentals of Heat and Mass Transfer*. John Wiley & Sons, Inc., 6th edition edition, 2006.

[38] S. Armstrong and W. G. Hurley. A thermal model for photovoltaic panels under varying atmospheric conditions. *Applied Thermal Engineering*, 30(11-12):1488–1495, 2010.

[39] Roland Pässler. Dispersion-related description of temperature dependencies of band gaps in semiconductors. *Physical Review B - Condensed Matter and Materials Physics*, 66(8):1–18, 2002.

[40] Yajie Jiang, Arman Mahboubi Soufiani, Angus Gentle, Fuzhi Huang, Anita Ho-Baillie, and Martin A. Green. Temperature dependent optical properties of CH 3 NH 3 PbI 3 perovskite by spectroscopic ellipsometry. *Applied Physics Letters*, 108(6):061905, feb 2016.

[41] A. Viúdez-Mora, M. Costa-Surós, J Calbó, and J A González. Modeling atmospheric longwave radiation at the surface during overcast skies: The role of cloud base height. *Journal of Geophysical Research: Atmospheres*, 120(1):199–214, jan 2015.

[42] Thomas Huld, Richard Müller, and Attilio Gambardella. A new solar radiation database for estimating PV performance in Europe and Africa. *Solar Energy*, 86(6):1803–1815, 2012.

[43] Dorota Matuszko. Influence of the extent and genera of cloud cover on solar radiation intensity. *International Journal of Climatology*, 32(15):2403–2414, 2012.

[44] Martin A. Green and Anita W.Y. Ho-Baillie. Pushing to the Limit: Radiative Efficiencies of Recent Mainstream and Emerging Solar Cells. *ACS Energy Letters*, 4(7):1639–1644, 2019.

[45] Matthias Müller, Gerd Fischer, Bernd Bitnar, Stefan Steckemetz, Roman Schiepe, Maria Mühlbauer, René Köhler, Philipp Richter, Christian Kusterer, Alexander Oehlke, Eric Schneiderlöchner, Hendrik Sträter, Franziska Wolny, Matthias Wagner, Phedon Palinginis, and D. Holger Neuhaus. Loss analysis of 22% efficient industrial PERC solar cells. *Energy Procedia*, 124:131–137, 2017.

[46] Thomas Kirchartz and Uwe Rau. What Makes a Good Solar Cell? *Advanced Energy Materials*, 8(28):1703385, oct 2018.